Generalized imaging conditions for wave-equation migration

Paul Sava* and Sergey Fomel†

* *Center for Wave Phenomena, Colorado School of Mines,Golden CO 80401, USA*
† *Bureau of Economic Geology, University of Texas (Austin), Austin, TX 78758, USA*

ABSTRACT

A typical imaging condition for seismic reflection data involves source and receiver wavefield matching, e.g. by cross-correlation, at every image location. This statement is true no matter how the two wavefields are reconstructed, for example by one-way wavefield extrapolation, or two-way reverse-time extrapolation, or Kirchhoff integral methods. This statement is also true when the source and receiver wavefields are reconstructed using different velocity models, as is the case for imaging of converted waves. Angle-dependent reflectivity information can be extracted from the source and receiver wavefield by retaining multiple lags of the imaging cross-correlation, i.e. by analyzing the match of wavefields shifted relative to one-another. Wavefields can be shifted in space (3D) or in time (1D), and each shift method has an associated angle-decomposition method. This paper explores the various types of imaging condition using space and time shifts and derives relations for angle decomposition for converted-wave imaging using time-shifts.

Key words: imaging condition, converted waves.

1 INTRODUCTION

A key challenge for imaging in complex areas is accurate determination of a velocity model in the area under investigation. Migration velocity analysis is based on the principle that image accuracy indicators are optimized when data are correctly imaged. A common procedure for velocity analysis is to examine the alignment of images created with multi-offset data. An optimal choice of image analysis can be done in the angle domain which is free of some complicated artifacts present in surface offset gathers in complex areas (Stolk and Symes, 2002).

Migration velocity analysis after migration by wavefield extrapolation requires image decomposition in scattering angles relative to reflector normals. Several methods have been proposed for such decompositions (de Bruin et al., 1990; Prucha et al., 1999; Mosher and Foster, 2000; Rickett and Sava, 2002; Xie and Wu, 2002; Sava and Fomel, 2003; Soubaras, 2003; Fomel, 2004; Biondi and Symes, 2004). These procedures require decomposition of extrapolated wavefields in variables that are related to the reflection angle.

A key component of such image decompositions is the imaging condition. A careful implementation of the imaging condition preserves all information necessary to decompose images in their angle-dependent components. The challenge is efficient and reliable construction of these angle-dependent images for velocity or amplitude analysis.

In migration with wavefield extrapolation, a prestack imaging condition based on spatial shifts of the source and receiver wavefields allows for angle-decomposition (Rickett and Sava, 2002; Sava and Fomel, 2005a). Such formed angle-gathers describe reflectivity as a function of reflection angles and are powerful tools for migration velocity analysis (MVA) or amplitude versus angle analysis (AVA). However, due to the large expense of space-time cross-correlations, especially in three dimensions, this imaging methodology is not used routinely in data processing.

A different form of imaging condition involves time-shifts instead of space-shifts between wavefields computed from sources and receivers. Similarly to the space-shift imaging condition, an image is built by space-time

cross-correlations of subsurface wavefields, and multiple lags of the time cross-correlation are preserved in the image. Time-shifts have physical meaning that can be related directly to reflection geometry, similarly to the procedure used for space-shifts. Furthermore, time-shift imaging is cheaper to apply than space-shift imaging, and thus it might alleviate some of the difficulties posed by costly cross-correlations in 3D space-shift imaging condition.

The idea of a time-shift imaging condition is related to the idea of depth focusing analysis (Faye and Jeannot, 1986; MacKay and Abma, 1992; MacKay and Abma, 1993; Nemeth, 1995; Nemeth, 1996).

The time-shift imaging concept is applicable to Kirchhoff migration, migration by wavefield extrapolation, or reverse-time migration. This concept is also applicable to migration of single-mode (PP) or converted-mode (PS) waves. In this paper, we develop the theory and show examples of angle decomposition after time-shift imaging of converted waves. All formulas developed for this purpose reduce to the previously-derived formulas for decomposition of single-mode images.

2 IMAGING CONDITION

If we make the assumption that seismic data consists of singly-scattered reflections, we can describe migration as a succession of two steps:

(i) **Wavefield extrapolation**, in which step we construct source and receiver wavefields from synthetic or recorded data. The source and receiver wavefields are four-dimensional objects denoted by the symbols $\mathbf{u}_s(\mathbf{m},t)$ and $\mathbf{u}_r(\mathbf{m},t)$, where $\mathbf{m}$ indicates position in a three-dimensional space, and t indicates time. In typical migration procedures, the four-dimensional objects $\mathbf{u}_s$ and $\mathbf{u}_r$ are not stored explicitly, but they are computed on-the-fly as needed for imaging at a given position $\mathbf{m}$ in space.

(ii) **Imaging condition**, in which step we extract reflectivity information by comparing the source and receiver wavefields. A useful imaging condition produces a map of reflectivity at all locations in space, function of angles of incidence and reflection. This information can be employed in migration velocity analysis (MVA) and amplitude-versus-angle analysis (AVA).

We can distinguish two parts of an imaging condition: wavefield comparison and angle-decomposition. In the first part, we explore the match of source and receiver wavefields and build objects containing reflectivity information. Cross-correlation at every location in space is an example of wavefield comparison. In the second part, we extract the actual angle-dependent reflectivity information from images produced by space-time wavefield cross-correlation.

We can look at an imaging procedure formulated in this framework as an exercise in matching of two four-dimensional objects. Fundamentally, there is no difference between the four coordinate axes, except for their physical meaning. We can exploit this similitude of coordinate axes in formulating generic wavefield comparison procedures. Deconvolution or cross-correlation are just two particular options.

Angle-decomposition, however, requires physical interpretation of the four coordinate axes to extract meaningful information about reflection angles. We exploit those physical relations to derive the formulas presented in this paper.

All types of migration procedures for single-mode (PP) waves, including Kirchhoff migration, migration by wavefield extrapolation, reverse-time migration etc. can be formulated in this framework. This framework is also applicable to imaging of converted waves, except that wavefield extrapolation on the receiver side uses the velocity of the S-waves resulted after conversion at reflectors in depth.

The main topic of this paper is to formulate imaging conditions for single-mode and converted-mode waves starting from the four-dimensional source and receiver wavefields. We describe several options for source-receiver wavefield comparison by space-time cross-correlations, followed by specific angle-decompositions.

2.1 Conventional imaging condition

A conventional imaging condition for shot-record migration, also known as $U\overline{D}$ imaging condition (Claerbout, 1985), consists of time cross-correlation at every image location between the source and receiver wavefields, followed by image extraction at zero time. Mathematically, we can represent this process by the relations

$$\mathbf{u}\left(\mathbf{m},t\right) = \mathbf{u}_s\left(\mathbf{m},t\right) \star \mathbf{u}_r\left(\mathbf{m},t\right) \ , \tag{1}$$

$$\mathbf{R}\left(\mathbf{m}\right) = \mathbf{u}\left(\mathbf{m},t=0\right) \ . \tag{2}$$

Here, $\mathbf{m} = [m_x, m_y, m_z]$ is a vector describing the locations of image points, $\mathbf{u}_s(\mathbf{m},t)$ and $\mathbf{u}_r(\mathbf{m},t)$ are source and receiver wavefields respectively, and $\mathbf{R}(\mathbf{m})$ denotes the migrated image, proportional to reflectivity at every location in space. The symbol $\star$ denotes cross-correlation in time.

A typical implementation of this imaging condition is in the Fourier domain, where the image is produced using the expression

$$\mathbf{R}\left(\mathbf{m},\right) = \sum_{\omega} \mathbf{U}_s\left(\mathbf{m},\omega\right) \overline{\mathbf{U}_r\left(\mathbf{m},\omega\right)} \ , \tag{3}$$

where summation over frequency ω corresponds to imaging at zero time. The over-line represents a complex conjugate applied on the receiver wavefield $\mathbf{U}_r$ in the Fourier domain.

2.2 Space-shift imaging condition

Another more general imaging condition (Sava and Fomel, 2005a) estimates image reflectivity using the expressions:

$$\mathbf{u}\left(\mathbf{m},\mathbf{h},t\right) = \mathbf{u}_s\left(\mathbf{m}-\mathbf{h},t\right) \star \mathbf{u}_r\left(\mathbf{m}+\mathbf{h},t\right) \ , \quad (4)$$

$$\mathbf{R}\left(\mathbf{m},\mathbf{h}\right) = \mathbf{u}\left(\mathbf{m},\mathbf{h},t=0\right) \ . \quad (5)$$

Here, $\mathbf{h} = [h_x, h_y, h_z]$ is a vector describing the local source-receiver separation in the image space.

In this imaging condition, we do not assume that the source and receiver wavefields maximize image strength at the spatial zero-lag of the cross-correlation, sometimes referred to as zero-offset (Claerbout, 1985). Since $\mathbf{h}$ is a 3D vector, zero-lag refers to setting all its three components to zero. Instead, we probe other lags of the cross-correlation which may maximize image strength in cases of inaccurate wavefield extrapolation caused either by inaccurate velocity or inaccurate algorithms.

This imaging condition can also be implemented in the Fourier domain using the expression

$$\mathbf{R}\left(\mathbf{m},\mathbf{h}\right) = \sum_{\omega} \mathbf{U}_s\left(\mathbf{m}-\mathbf{h},\omega\right) \overline{\mathbf{U}_r\left(\mathbf{m}+\mathbf{h},\omega\right)} \ , \quad (6)$$

which simply involves summation over frequency ω for imaging at zero time.

2.3 Time-shift imaging condition

Another possible imaging condition involves cross-correlation of the source and receiver wavefields shifted in time, as opposed to space. Mathematically, we can represent this process by the relations

$$\mathbf{u}\left(\mathbf{m},t,\tau\right) = \mathbf{u}_s\left(\mathbf{m},t-\tau\right) \star \mathbf{u}_r\left(\mathbf{m},t+\tau\right) \ , \quad (7)$$

$$\mathbf{R}\left(\mathbf{m},\tau\right) = \mathbf{u}\left(\mathbf{m},\tau,t=0\right) \ . \quad (8)$$

Here, τ is a time shift between the source and receiver wavefields prior to imaging.

This imaging condition is similar to the space-shift option, except that here we probe in time as opposed to space the situations in which the source and receiver wavefields match at an image location. With this imaging condition, we exploit the four-dimensional nature of the source and receiver wavefields: there is no difference, in principle, between the time and space coordinates.

This imaging condition can also be implemented in the Fourier domain using the expression

$$\mathbf{R}\left(\mathbf{m},\tau\right) = \sum_{\omega} \mathbf{U}_s\left(\mathbf{m},\omega\right) \overline{\mathbf{U}_r\left(\mathbf{m},\omega\right)} e^{2i\omega\tau} \ , \quad (9)$$

which simply involves a phase-shift applied to the wavefields prior to summation over frequency ω for imaging at zero time.

2.4 Dual-shift imaging condition

Using the same approach as for the preceding procedures, the most general imaging condition we can formulate in this generic family involves cross-correlation of the source and receiver wavefields after shifting in both time and space. Mathematically, we can represent this process by the relations

$$\mathbf{u}\left(\mathbf{m},\mathbf{h},t,\tau\right) = \mathbf{u}_s\left(\mathbf{m}-\mathbf{h},t-\tau\right) \star \mathbf{u}_r\left(\mathbf{m}+\mathbf{h},t+\tau\right) \ , \quad (10)$$

$$\mathbf{R}\left(\mathbf{m},\mathbf{h},\tau\right) = \mathbf{u}\left(\mathbf{m},\mathbf{h},\tau,t=0\right) \ . \quad (11)$$

In this imaging condition we probe wavefield similitude using both shifting in space and time. Thus, this imaging covers the preceding imaging conditions as special cases, either when $\tau = 0$, equation (4),or when $\mathbf{h} = 0$, equation (7).

This imaging condition can also be implemented in the Fourier domain using the expression

$$\mathbf{R}\left(\mathbf{m},\mathbf{h},\tau\right) = \sum_{\omega} \mathbf{U}_s\left(\mathbf{m}-\mathbf{h},\omega\right) \overline{\mathbf{U}_r\left(\mathbf{m}-\mathbf{h},\omega\right)} e^{2i\omega\tau} \ . \quad (12)$$

The imaging procedures described in this section produce images that have the potential to be used for angle decomposition of reflectivity at every image location in order to make this imaging useful for MVA or AVA.

The imaging conditions presented in this section make no assumption on the nature of the source and receiver wavefields We can reconstruct those two wavefields using any type of extrapolation, or using different models for the source and receiver wavefields.

In the following section, we discuss angle-decomposition based on the images obtained by conditions described in the current section. For angle decomposition, we cannot ignore anymore the physical nature of the two wavefields we are comparing, and we need to specify what type of wave (P or S) do the various wavefields correspond to. For the following analysis, we will assume that source wavefields correspond to incident P waves, and receiver wavefield correspond to reflected S waves.

3 ANGLE DECOMPOSITION

We can develop procedures for angle-decomposition starting from the multi-lag cross-correlations constructed in the preceding section. At this stage, we need to exploit the physical meaning of the various lags, either along space axes or along the time axis. In general, 3-D angle-decomposition should define reflectivity function of reflection and azimuth angles. In this paper, we concentrate on decomposition function of the reflection angle only.

Using the definitions introduced in the preceding section, we can make the standard notations for source and receiver coordinates, respectively: $\mathbf{s} = \mathbf{m} - \mathbf{h}$ and

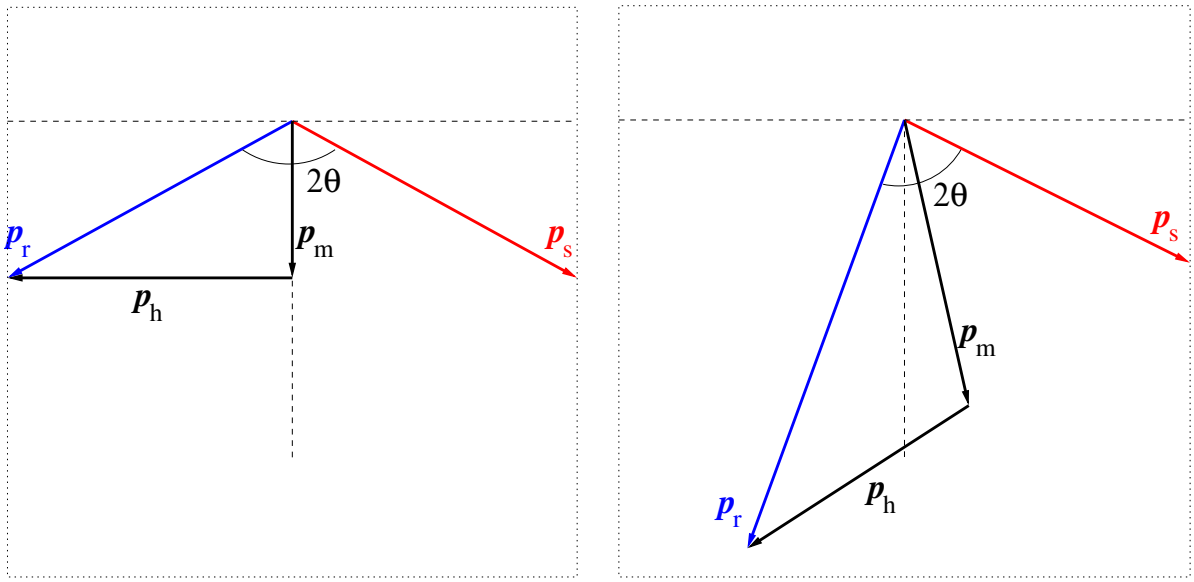

(a) (b)

Figure 1. Geometric relations between ray vectors at a reflection point. Single-mode (PP) case (a), and Converted-mode (PS) case (b).

$\mathbf{r} = \mathbf{m} + \mathbf{h}$. The traveltime from a source to a receiver is a function of all spatial coordinates of the seismic experiment $t = t(\mathbf{m}, \mathbf{h})$. Suppose we could identify the function $t(\mathbf{m}, \mathbf{h})$, then differentiating t with respect to all components of the vectors $\mathbf{m}$ and $\mathbf{h}$, and using the standard notations $\mathbf{p}_\alpha = \nabla_\alpha t$, where $\alpha = \{\mathbf{m}, \mathbf{h}, \mathbf{s}, \mathbf{r}\}$, we can write $2\mathbf{p_m} = \mathbf{p_r} + \mathbf{p_s}$ and $2\mathbf{p_h} = \mathbf{p_r} - \mathbf{p_s}$. Therefore, we can also write equivalent relations $\mathbf{p_s} = \mathbf{p_m} - \mathbf{p_h}$ and $\mathbf{p_r} = \mathbf{p_m} + \mathbf{p_h}$.

By analyzing the geometric relations of various vectors at an image point, Figures 1(a) and 1(b), we can write the following trigonometric expressions:

$$4|\mathbf{p_h}|^2 = |\mathbf{p_s}|^2 + |\mathbf{p_r}|^2 - 2|\mathbf{p_s}||\mathbf{p_r}|\cos(2\theta) \ , \quad (13)$$

$$4|\mathbf{p_m}|^2 = |\mathbf{p_s}|^2 + |\mathbf{p_r}|^2 + 2|\mathbf{p_s}||\mathbf{p_r}|\cos(2\theta) \ . \quad (14)$$

Therefore, from equations (13)-(14)we can write:

$$4|\mathbf{p_h}|^2 + 4|\mathbf{p_m}|^2 = 2|\mathbf{p_s}|^2 + 2|\mathbf{p_r}|^2 \ . \quad (15)$$

3.1 Space-shift angle decomposition for single-mode waves

Defining $\mathbf{k_m}$ and $\mathbf{k_h}$ as location and offset wavenumber vectors, and assuming $|\mathbf{p_s}| = |\mathbf{p_r}| = s$, where $s(\mathbf{m})$ is the slowness at image locations, we can write

$$4|\mathbf{p_h}|^2 = 2s^2(1 - \cos 2\theta) \ , \quad (16)$$

$$4|\mathbf{p_m}|^2 = 2s^2(1 + \cos 2\theta) \ . \quad (17)$$

If we eliminate ω and make the notations $|\mathbf{k_h}| = |\mathbf{p_h}|/\omega$ and $|\mathbf{k_m}| = |\mathbf{p_m}|/\omega$, we obtain the expression

$$\tan^2\theta = \frac{|\mathbf{k_h}|^2}{|\mathbf{k_m}|^2} \ , \quad (18)$$

that can be used for angle decomposition for single-mode waves after space-shift imaging condition (Sava and Fomel, 2005a).

3.2 Time-shift angle decomposition for single-mode waves

Using the same definitions for $|\mathbf{p_s}|$ and $|\mathbf{p_r}|$ as in the preceding subsection, we can transform equation (14) to the form

$$4|\mathbf{p_m}|^2 = 2s^2(1 + \cos 2\theta) \ , \quad (19)$$

therefore, we can write the expression

$$\cos^2\theta = \frac{|\mathbf{p_m}|^2}{s^2} \ , \quad (20)$$

which can be used for angle decomposition for single-mode waves after time-shift imaging condition.

Similarly, we can transform equation (13)

$$4|\mathbf{p_h}|^2 = 2s^2(1 - \cos 2\theta) \ , \quad (21)$$

therefore, we can write the expression

$$\sin^2\theta = \frac{|\mathbf{p_h}|^2}{s^2} \ , \quad (22)$$

which can be used for angle decomposition for single-mode waves after time-shift imaging condition.

3.3 Space-shift angle decomposition for converted waves

We can transform the expressions (13)-(14) using the notations $|\mathbf{p_s}| = s$ and $|\mathbf{p_r}| = \gamma s$, where $\gamma(\mathbf{m})$ is the v_p/v_s ratio, and $s(\mathbf{m})$ is the slowness associated with the incoming ray at every image point:

$$4|\mathbf{p_h}|^2 = s^2\left(1+\gamma^2-2\gamma\cos 2\theta\right) , \quad (23)$$

$$4|\mathbf{p_m}|^2 = s^2\left(1+\gamma^2+2\gamma\cos 2\theta\right) . \quad (24)$$

If we eliminate ω and make the notations $|\mathbf{k_h}| = |\mathbf{p_h}|/\omega$ and $|\mathbf{k_m}| = |\mathbf{p_m}|/\omega$, we obtain the expression

$$\tan^2\theta = \frac{(1+\gamma)^2|\mathbf{k_h}|^2-(1-\gamma)^2|\mathbf{k_m}|^2}{(1+\gamma)^2|\mathbf{k_m}|^2-(1-\gamma)^2|\mathbf{k_h}|^2} , \quad (25)$$

that can be used for angle decomposition for converted waves after space-shift imaging condition.

3.4 Time-shift angle decomposition for converted waves

Using the same definitions for $|\mathbf{p_s}|$ and $|\mathbf{p_r}|$ as in the preceding subsection, we can transform equation (14)

$$4|\mathbf{p_m}|^2 = s^2\left(1+\gamma^2+2\gamma\cos 2\theta\right) , \quad (26)$$

therefore we can write

$$\cos^2\theta = \frac{1}{\gamma}\frac{|\mathbf{p_m}|^2}{s^2}-\frac{(1-\gamma)^2}{4\gamma} . \quad (27)$$

When $\gamma = 1$ (P waves), this expression reduces to

$$\cos\theta = \frac{|\mathbf{p_m}|}{s} . \quad (28)$$

Similarly, we can transform the equation (13)

$$4|\mathbf{p_h}|^2 = s^2\left(1+\gamma^2-2\gamma\cos 2\theta\right) , \quad (29)$$

therefore we can write

$$\sin^2\theta = \frac{1}{\gamma}\frac{|\mathbf{p_h}|^2}{s^2}-\frac{(1-\gamma)^2}{4\gamma} . \quad (30)$$

When $\gamma = 1$ (P waves), this expression reduces to

$$\sin\theta = \frac{|\mathbf{p_h}|}{s} . \quad (31)$$

4 ALGORITHMS

In the most general case described in this paper, a seismic image is a multi-dimensional object function of position $\mathbf{m}$, space-shift $\mathbf{h}$ and time-shift τ, $\mathbf{R}(\mathbf{m},\mathbf{h},\tau)$. We can use the relations between space and time coordinates developed in the preceding section to define various angle-decomposition algorithms. Since $\mathbf{R}(\mathbf{m},\mathbf{h},\tau)$ is a large object that is unlikely, in practice, to be computed or stored completely, we design algorithms involving subsets of this large image:

- If we construct a seismic image using only space-shift

$$\mathbf{R}(\mathbf{m},\mathbf{h}) ,$$

we use equations (18) or (25) for angle decomposition of single-mode waves or converted-mode waves, respectively. The computation and storage requirements are high, since we need to store images for 3-D cross-correlation lags. However, if only the reflection angle is of interest, we can reduce cost by storing only the absolute value of the space-shift vector (Sava and Fomel, 2005a; Sava and Fomel, 2005b)
A decomposition algorithm is a follows:

$$\mathbf{R}(\mathbf{m},\mathbf{h}) \rightarrow \mathbf{R}(\mathbf{k_m},\mathbf{k_h}) \rightarrow \mathbf{R}(\mathbf{k_m},|\mathbf{k_h}|/|\mathbf{k_m}|) \rightarrow \mathbf{R}(\mathbf{m},\theta)$$

where each arrow indicates a transformation from one domain to another, and $\mathbf{k_m}$ and $\mathbf{k_h}$ are the Fourier duals of position $\mathbf{m}$ and space-shift $\mathbf{h}$. The transform from $(\mathbf{m},\mathbf{h})$ to $(\mathbf{k_m},\mathbf{k_h})$ and back represent Fourier transforms, and the transformation from $(\mathbf{k_m},\mathbf{k_h})$ to $(\mathbf{k_m},|\mathbf{k_h}|/|\mathbf{k_m}|)$ represents slant-stacking. For converted waves, the decomposition from the slant-stack parameter $|\mathbf{k_h}|/|\mathbf{k_m}|$ requires a space-domain correction based on the v_p/v_s ratio.

- If we construct a seismic image using only time-shift

$$\mathbf{R}(\mathbf{m},\tau) ,$$

we use equations (20) or (27) for angle decomposition of single-mode waves or converted-mode waves, respectively. The computation and storage requirements are small, since we need to store images for 1-D cross-correlation lags. However, although the cost is smaller, we lose the option of computing the azimuth of the reflection and we are limited only to the reflection angle. A decomposition algorithm is a follows:

$$\mathbf{R}(\mathbf{m},\tau) \rightarrow \mathbf{R}(\mathbf{k_m},\omega) \rightarrow \mathbf{R}(\mathbf{k_m},|\mathbf{k_m}|/\omega) \rightarrow \mathbf{R}(\mathbf{m},\theta)$$

where $\mathbf{k_m}$ and ω are the Fourier duals of position $\mathbf{m}$ and time-shift τ. For converted waves, the decomposition from the slant-stack parameter $|\mathbf{k_m}|/\omega$ requires a space-domain correction based on the slowness s and the v_p/v_s ratio.

- If we construct a seismic image using space-shift and time-shift at selected positions (e.g. along predefined horizons indicated by positions $\mathbf{m}_0$),

$$\mathbf{R}(\mathbf{m}_0,\mathbf{h},\tau) ,$$

we can use equations (22) or (30) for angle decomposition of single-mode waves or converted-mode waves, respectively. The computations and storage requirements are small, since we are not computing and storing space and time cross-correlation lags at all locations in the image, but only at a small subset of positions. Such an approach is valid for cases in which we need to analyze angle-dependent reflectivity only along horizons,

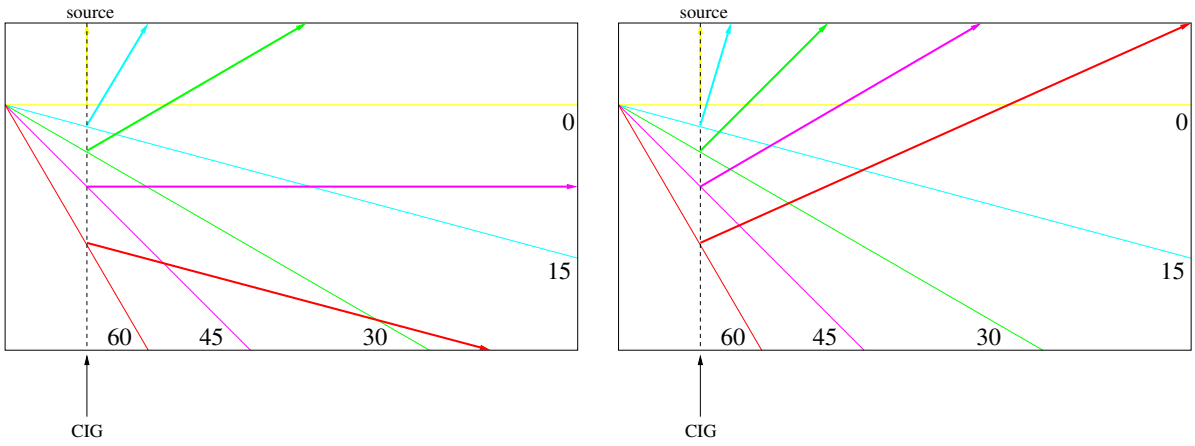

Figure 2. Synthetic seismic experiment: PP reflection geometry (a) and PS reflection geometry (b).

e.g. for azimuthal variation of reflectivity caused by azimuthal anisotropy. The subject of angle-decomposition for anisotropic propagation falls outside the scope of this paper, although it is closely related with the analysis done here.
A decomposition algorithm is a follows:

$$\mathbf{R}(\mathbf{m}_0,\mathbf{h},\tau) \rightarrow \mathbf{R}(\mathbf{m}_0,\mathbf{k_h},\omega) \rightarrow \mathbf{R}(\mathbf{m}_0,|\mathbf{k_h}|/\omega) \rightarrow \mathbf{R}(\mathbf{m}_0,\theta)$$

where $\mathbf{k_h}$ and ω are the Fourier duals of space-shift $\mathbf{h}$ and time-shift τ. For converted waves, the decomposition from the slant-stack parameter $|\mathbf{k_h}|/\omega$ requires a space-domain correction based on the slowness s and the v_p/v_s ratio.

5 EXAMPLE

We illustrate the imaging and angle-decomposition methods derived in this paper with a synthetic example. The reflectivity model consists of five reflectors of increasing slopes, from 0° to 60°, as illustrated in Figures 2(a) and 2(b). In this experiment, the P-wave velocity is $v_p = 3200$ m/s and the S-wave velocity is $v_s = 800$ m/s. We chose those velocities in order to capture reflections off the steeper dipping reflectors in a reasonable acquisition geometry. In this experiment, we analyze one common-image gather located at the same horizontal position as the surface seismic source. In this way, the reflector dip is equal to the angle of incidence on each reflector.

Figure 2(a) shows a schematic of a single-mode (PP) experiment. Given the constant velocity of the model, the single-mode data from the reflector dipping more than 45° are not recorded at the surface. In contrast, the converted-mode data from all reflectors are recorded at the surface. Figure 2(b) shows a schematic of the converted-mode (PS) experiment.

Figure 3 shows the converted-mode seismic data from all five reflectors. We analyze the positive offsets of the seismic data which contain the reflections from the interfaces in the model.

We migrate this shot using one-way wavefield extrapolation using space-shift and time-shift imaging conditions. Figure 4 shows the migrated image at zero shift. As predicted by theory, this image is identical for both space-shift and time-shift imaging conditions when the values of the shift is zero. Therefore, we are showing only one of the two images.

Figures 5(a)-5(c) show different views of the common-image gather (CIG) located at the same horizontal location as the source $x = 1000$ m. Panel (a) depicts the CIG resulting from the space-shift imaging condition. The vertical axis represents depth z and the horizontal axis represents horizontal space shift labeled, for simplicity, h. Panel (b) depicts the same CIG after slant-stack in the $z-h$ space. The horizontal axis is the slant-stack parameter, which is related to the reflection angle at every reflector, except for a correction based on dip and the v_p/v_s ratio. Panel (c) depicts the same CIG after transformation to reflection angle θ using local values of P and S velocities, as well as a correction for the structural dip measured on the migrated image depicted in Figure 4. As expected, each reflector is represented in this final plot at a specific angle of incidence. The vertical lines indicate the correct reflection angles of converted waves reflecting from the interfaces dipping at angles between 0° and 60°.

Figures 6(a)-6(c) show a similar analysis the the one in Figures 5(a)-5(c) but for imaging using time-shift. Panel (a) depicts one CIG at $x = 1000$ m, panel (b)

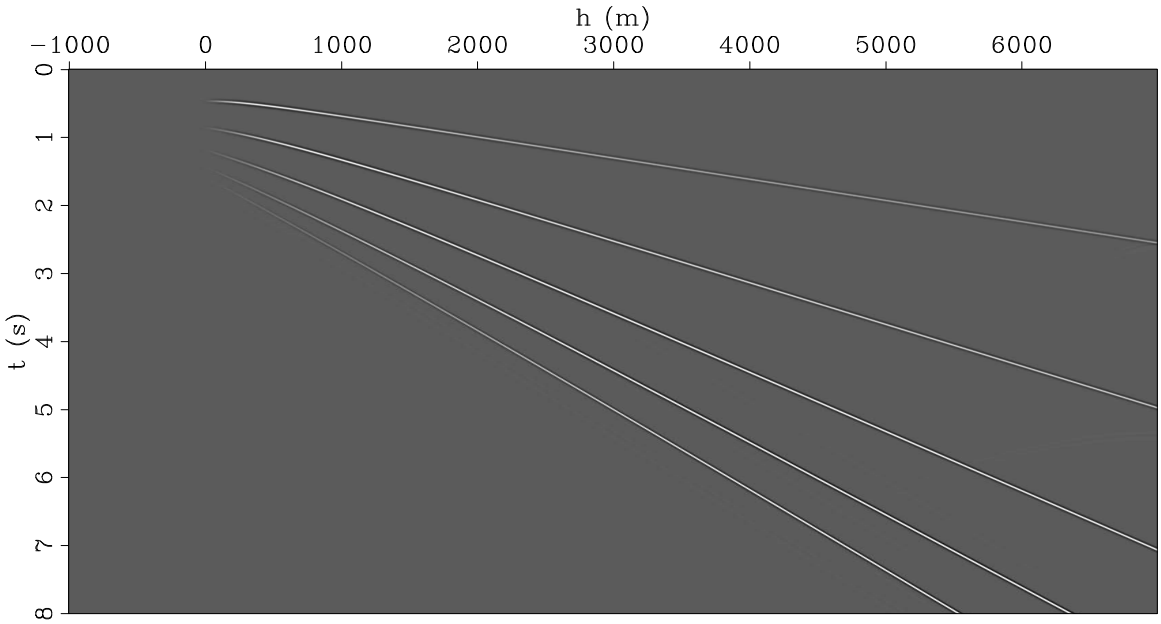

Figure 3. Synthetic PS reflection data

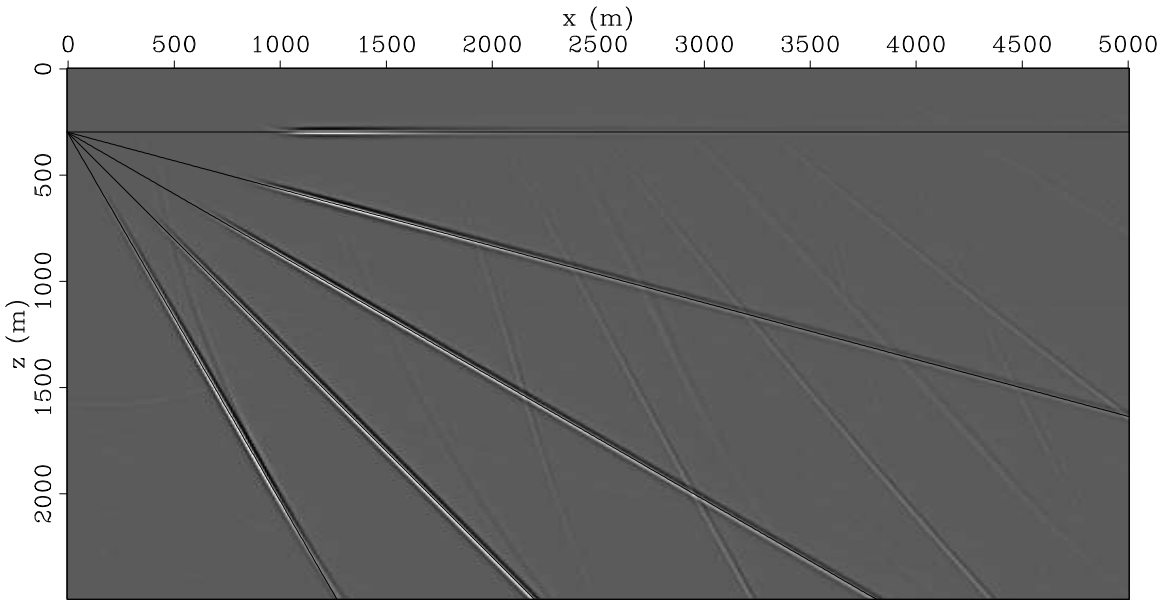

Figure 4. Migrated images for PS data

depicts the CIG after slant-stack in the $z - \tau$ space, and panel (c) depicts the CIG after transformation to reflection angle, including the space-domain corrections for structural dip and v_p/v_s ratio.

As for the space-shift images, the energy corresponding to every reflector from the CIG obtained by time-shift imaging concentrates well in the slant-stack panels, Figures5(b) and 6(b). However, a striking difference occurs in the $z - \theta$ panels: while the energy for every reflector in Figure 5(c) concentrates well, the energy in Figure 6(c) is much less focused, particularly at small angles.

This phenomenon was observed and discussed in detail by Sava and Fomel (2006), and it is related to the lower angular resolution for time-shift imaging at small angles. This fact is illustrated in Figures 7(a)-7(b) depicting impulse response transformations for time-shift imaging: panel (a) depicts various events in a slant-stack

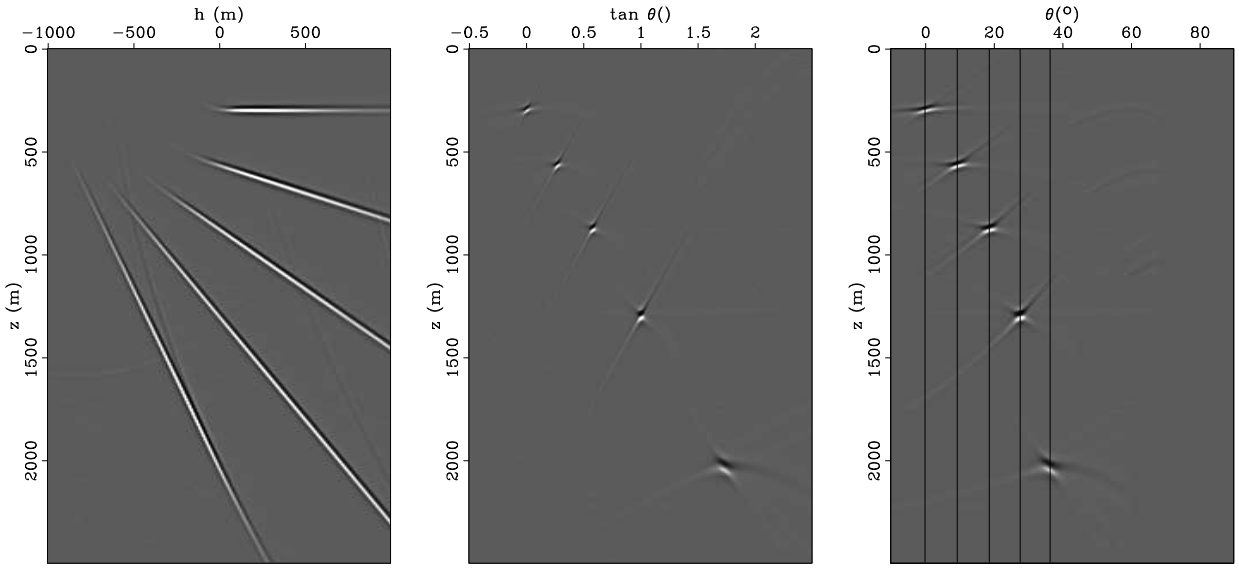

(a) (b) (c)

Figure 5. Common-image gather at $x = 1000$ m for space-shift imaging condition: common-image gather (a), slant-stack gather (b) and common-angle gather (c).

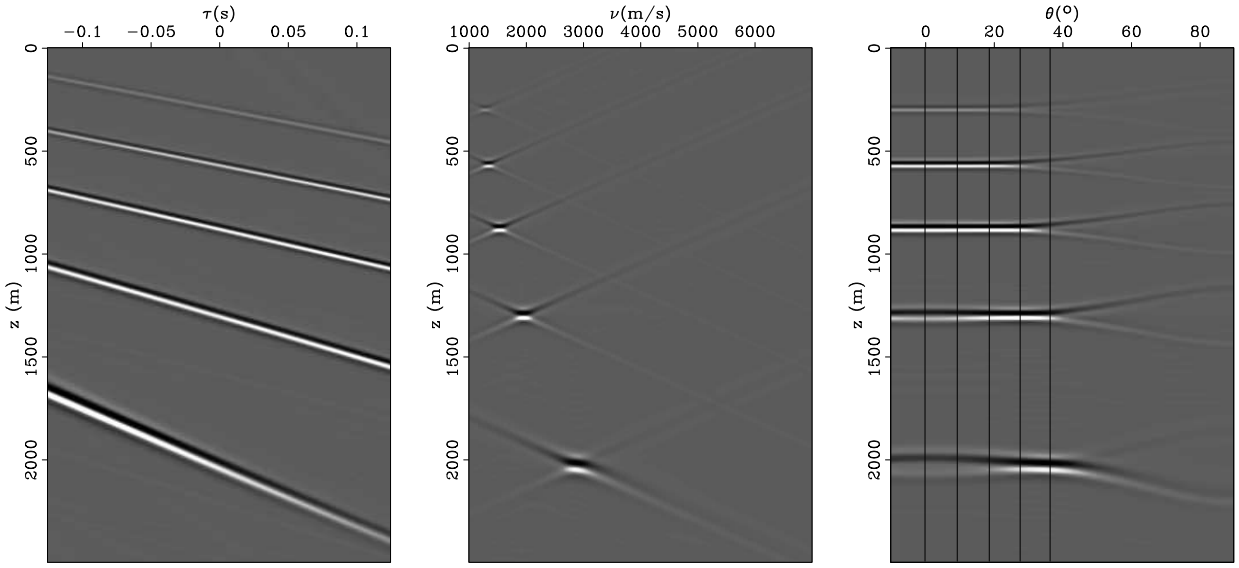

(a) (b) (c)

Figure 6. Common-image gather at $x = 1000$ m for time-shift imaging condition: common-image gather (a), slant-stack gather (b) and common-angle gather (c).

panel, similar to Figure 6(b), and panel (b) depicts the same events in a reflection angle panel, similar to Figure 6(c). At low reflection angles, the angular resolution is low, but it increases at large reflection angles to levels comparable with those of reflections mapped using space-shift imaging. The simple explanation for this phenomenon is that the space-shift transformation involves the $\tan\theta$ trigonometric function whose slope at $\theta \to 0$ is equal to 1, while the time-shift transformation involves the $\cos\theta$ function whose slope at $\theta \to 0$ is equal to 0. Thus, even given equivalent slant-stack resolutions, the angle resolution around $\theta = 0$ is much poorer for time-shift imaging than for space-shift imaging simply because of the use of a different trigonometric function.

6 CONCLUSIONS

We develop imaging conditions for converted waves based on time-shifts between source and receiver wavefields. This method is applicable to Kirchhoff, reverse-time and wave-equation migrations and produces common-image gathers indicative of velocity errors. In wave-equation migration, time-shift imaging is more efficient than space-shift imaging, since it only involves a simple phase shift prior to the application of the usual imaging cross-correlation. Disk storage is also reduced, since the output volume depends on only one parameter (time-shift τ) instead of three parameters (space-shift $\mathbf{h}$). We show how this imaging condition can be used to construct angle-gathers from time-shift gathers. Although time-shift imaging is, in principle, capable of representing the same information as space-shift imaging, in practice the angular resolution of the angle decomposition for time-shift is much lower than the one for space shift. This inconvenience needs to be addressed by future research.

7 ACKNOWLEDGMENT

We would like to acknowledge ExxonMobil for partial financial support of this research.

REFERENCES

Biondi, B., and Sava, P., 1999, Wave-equation migration velocity analysis *in* 69th Ann. Internat. Mtg. Soc. of Expl. Geophys., 1723–1726.

Biondi, B., and Symes, W. W., 2004, Angle-domain common-image gathers for migration velocity analysis by wavefield-continuation imaging: Geophysics, **69**, 1283–1298.

de Bruin, C. G. M., Wapenaar, C. P. A., and Berkhout, A. J., 1990, Angle-dependent reflectivity by means of prestack migration: Geophysics, **55**, 1223–1234.

Claerbout, J. F., 1985, Imaging the Earth's Interior: Blackwell Scientific Publications.

Faye, J. P., and Jeannot, J. P., 1986, Prestack migration velocities from focusing depth analysis *in* 56th Ann. Internat. Mtg. Soc. of Expl. Geophys., Session:S7.6.

Fomel, S., 2004, Theory of 3-D angle gathers in wave-equation imaging *in* 74th Ann. Internat. Mtg. Soc. of Expl. Geophys.

MacKay, S., and Abma, R., 1992, Imaging and velocity estimation with depth-focusing analysis: Geophysics, **57**, 1608–1622.

—, 1993, Depth-focusing analysis using a wavefront-curvature criterion: Geophysics, **58**, 1148–1156.

Mosher, C., and Foster, D., 2000, Common angle imaging conditions for prestack depth migration *in* 70th Ann. Internat. Mtg. Soc. of Expl. Geophys., 830–833.

Nemeth, T., 1995, Velocity estimation using tomographic depth-focusing analysis *in* 65th Ann. Internat. Mtg. Soc. of Expl. Geophys., 465–468.

—, 1996, Relating depth-focusing analysis to migration velocity analysis *in* 66th Ann. Internat. Mtg. Soc. of Expl. Geophys., 463–466.

Prucha, M., Biondi, B., and Symes, W., 1999, Angle-domain common image gathers by wave-equation migration *in* 69th Ann. Internat. Mtg. Soc. of Expl. Geophys., 824–827.

Rickett, J. E., and Sava, P. C., 2002, Offset and angle-domain common image-point gathers for shot-profile migration: Geophysics, **67**, 883–889.

Sava, P., and Biondi, B., 2004a, Wave-equation migration velocity analysis - I: Theory: Geophysical Prospecting, **52**, 593–606.

—, 2004b, Wave-equation migration velocity analysis - II: Subsalt imaging examples: Geophysical Prospecting, **52**, 607–623.

Sava, P. C., and Fomel, S., 2003, Angle-domain common-image gathers by wavefield continuation methods: Geophysics, **68**, 1065–1074.

Sava, P., and Fomel, S., 2005a, Coordinate-independent angle-gathers for wave equation migration *in* 75th Ann. Internat. Mtg. Soc. of Expl. Geophys.

Sava, P., and Fomel, S., 2005b, Wave-equation common-angle gathers for converted waves *in* 75th Ann. Internat. Mtg. Soc. of Expl. Geophys.

Sava, P. C., and Fomel, S., 2004, Time-shift imaging in wave-equation migration: Geophysics, submitted for publication.

Soubaras, R., 2003, Angle gathers for shot-record migration by local harmonic decomposition *in* 73rd Ann. Internat. Mtg. Soc. of Expl. Geophys., 889–892.

Stolk, C., and Symes, W., 2002, Artifacts in Kirchhoff common image gathers *in* 72nd Ann. Internat. Mtg. Soc. of Expl. Geophys., 1129–1132.

Xie, X., and Wu, R., 2002, Extracting angle domain information from migrated wavefield *in* 72nd Ann. Internat. Mtg. Soc. of Expl. Geophys., 1360–1363.

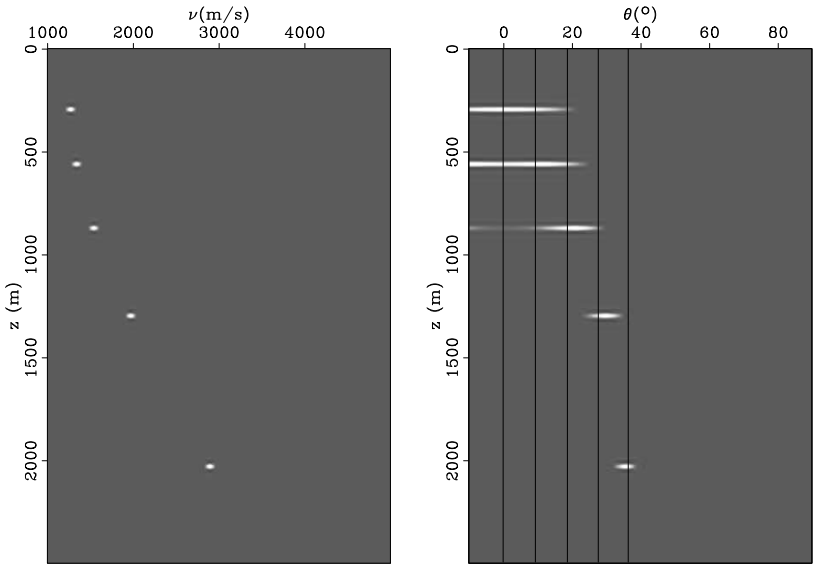

(a) (b)

Figure 7. Resolution experiment for time-shift imaging condition: simulated slant-stack (a) and angle-decomposition (b). Although the slant-stack is well focused for all events both function of depth z and slant-stack parameter ν, the resolution of the angle transformation is lower at small angles and higher at large angles.